Nanoscale Research Letters

NANO EXPRESS   **Open Access**

Synchrotron X-ray Absorption Spectroscopy Study of Local Structure in Al-Doped BiFeO₃ Powders

Turghunjan Gholam[1*], Li Rong Zheng[2], Jia Ou Wang[2], Hai Jie Qian[2], Rui Wu[2] and Hui-Qiong Wang[1*]

Abstract

The Al-doped BiFeO₃, i.e., BFA$_x$O powder samples with x = 0, 0.025, 0.05, and 0.1, were prepared via the hydrothermal route. The effects of Al substitution on the structural, electrical, and optical properties of BFA$_x$O samples were investigated. It is found that the substitution of Al ions at B-site of BiFeO₃ did not cause structural change and it still retains the rhombohedral perovskite structure with $R3c$ symmetry, which was confirmed by the X-ray diffraction (XRD) and Raman measurements. X-ray absorption fine structure (XAFS) above the Fe K-edge and Bi L_3-edge in BFA$_x$O powders was also measured and analyzed. Fe ions exhibit mixed valence states (Fe^{2+}/Fe^{3+}) while Bi ions keep the + 3 valence state in all the samples. Fe K-edge XAFS also indicated that there was a competition between hybridization of Fe 3d and Al 3d with O 2p orbitals and occurrence of the more 4p orbitals with Al doping. The Bi L_3-edge XAFS revealed that transition from 2$p_{3/2}$ to 6d state increased, so did the energy of 6d state. Besides, Al ion doping affected both the nearest-neighbor and next-nearest coordination shells of Fe atom and nearest-neighbor shells of Bi atom. Ultraviolet-visible (UV-Vis) spectroscopy results show the BFA$_x$O prepared by hydrothermal method could be an appropriate visible-light photocatalytic material.

Keywords: Hydrothermal route, X-ray absorption fine structure, BiFeO₃, Band gap

Background

Multiferroics are materials that simultaneously display ferroic properties, such as ferroelectricity, ferromagnetism, and ferroelasticity [1]. Such materials show interesting behaviors such as electrical polarization, which can be controlled with the application of an external electric field or vice-versa. Interest in these materials is owing to their wide applications in chemical biosensors, nanoelectronic and high-density data storage devices, etc [2, 3]. Perovskite structures have the general formula ABO₃, where O is an ion (refers to oxygen usually) and A and B are cations, respectively. Generally, A-site cation is larger with a lower valence state, which combines with O^{2-} to form a close-packed layer (i.e., at the corner of the unit cell). B-site cation is smaller with higher valence state, which can be adopted into an oxygen octahedral

coordination environment (i.e., at the center of an octahedron of oxygen anions) [4]. By definition, almost all the multiferroics are antiferromagnetic (AFM) or weak ferromagnetic (FM) with low transition temperatures. They are divided into two classes: single phase and composite. However, the single-phase multiferroic materials are rarely found in nature which shows the ferroelectric (FE) and FM properties concurrently [5]. Among all the multiferroic materials known today, bismuth ferrite (BiFeO₃; BFO) is one of the single-phase materials that have a rhombohedral distorted perovskite lattice type with polar space group $R3c$. BFO shows both FE with Curie temperature of $T_C \approx 1103$ k and G-type AFM ordering with Neel temperature of $T_N \approx 643$ k above room temperature (RT) [6]. This material exhibits the AFM G-type spin configuration along the $[111]_c$ or $[001]_h$ directions in its pseudo-cubic or rhombohedral structure and has a superimposed spiral spin structure with a periodicity of about 62 Å along the $[110]_h$ axis at RT [7]. It has a large intrinsic spontaneous polarization of about 90 μC/cm² ascribed to the distortion of octahedral FeO₆,

* Correspondence: turghunjan@stu.xmu.edu.cn; hqwang@xmu.edu.cn
[1]Key Laboratory of Semiconductors and Applications of Fujian Province, Collaborative Innovation Center for Optoelectronic Semiconductors and Efficient Devices, Department of Physics, Xiamen University, Xiamen 361005, People's Republic of China
Full list of author information is available at the end of the article

owing to the presence of 6 s^2 lone pair of electrons [8]. Furthermore, there is a magnetoelectric coupling between FE and magnetic order parameters. FE properties depend on the lone pair electrons, and FM properties rely on the partially filled inner shells, i.e., polarization comes from the Bi-site (A-site), while magnetization comes from the Fe-site (B-site).

Apart from above, unfortunately, the main disadvantages of BFO are its low resistivity or large leakage current, due to the charge defects such as bismuth and oxygen vacancies, impurity phases, valence fluctuations of iron, and poor interfacial quality [9]. In addition, it is difficult to obtain the high-quality BFO because of some impurity phases like $Bi_2Fe_4O_9$ (space group *Pbam*) and $Bi_{25}FeO_{39}$ (space group *I23*). It is inevitable that the impurities are generated in the process of preparation. To address these issues and limitations, several research groups have been using various methods to overcome the defects of BFO, e.g., strain modification, substitution of divalent and rare earth ion doping. Now, within this field of study, with rare earth element or transition metal ion doping at A-site or B-site, or co-doping at A and B-site, the multiferroic properties of BFO can be enhanced. For instance, doping with rare earth element can stabilize the perovskite structure, retain the non-centrosymmetry, and control the vaporization of Bi^{3+} ions [10]. Doping with transition metal ion can reduce the valence fluctuation of Fe^{3+} ions. Elements like Pr, Sm, Eu, Gd, and La [11, 12] for A-site substitution and Mn, Cr, and Ti [13–15] for B-site substitution have already been reported. Moreover, the magnetic, dielectric, and ferroelectric properties can be enhanced with co-doping. For the co-doping of A- and B-sites of BFO, La-Gd, Ba-Ni, Dy-Cr, Y-Mn, and Tb-Ti have been reported [16–20]. Until now, various routes including sol-gel [21], mechanochemical [22], auto-combustion [23], pulsed laser deposition [24], and hydrothermal [25, 26] have been reported to prepare BFO. The hydrothermal method has been widely applied owing to its energy saving, fine dispersion, low cost, and small particle size properties [27]. The reaction temperature should be high enough to form BFO and also used to remove the secondary phases during sample preparation. Most previous studies of Al doped at both A- and B-site of BFO have been investigated for structural, optical, and transport properties by Azam et al [28]. Madhu et al. [29] have reported the photocatalytic applications of B-site Al-doped BFO. Another report from Jawad et al. [30] explored the dielectric behavior of nanostructured BFO ceramics. The work of Wang et al. [31] studied the hollow crystals of Al-doped BFO in detail. However, some important physical properties are still lack of understanding, such as B-site doping effects on the local electronic structure of the materials. At the present stage, X-ray absorption fine structure spectroscopy (XAFS) is one of the powerful ways to study the local environment of an atom and provides structural information of the materials, as well as absorption energy, element valence state, charge transfer, and type of bonding [32]. To the best of our knowledge, there are no found reports on the effect of Al doping at B-site on the local electronic structure of BFO investigation by XAFS.

In this work, the undoped BFO and target compositions $BiFe_{1-x}Al_xO_3$ (BFA_xO) with x = 0, 0.025, 0.05, and 0.1 were synthesized via hydrothermal route. The main focus is on the investigation of the effect of Al doping at B-site on the properties of BFO which are compared with undoped BFO. The structural properties were investigated in detail.

Methods

The hydrothermal method was used to obtain undoped BFO and BFA_xO samples. Chemical reagents used in this work were bismuth nitrate ($Bi(NO_3)_3 \cdot 5H_2O$), iron nitrate ($Fe(NO_3)_3 \cdot 9H_2O$), aluminum nitrate ($Al(NO_3)_3 \cdot 6H_2O$), and potassium hydroxide (KOH). All chemical reagents were used as received without further purification. $Bi(NO_3)_3 \cdot 5H_2O$ and $Fe(NO_3)_3 \cdot 9H_2O$ were used as the source materials, while $Al(NO_3)_3 \cdot 6H_2O$ and KOH were used as additives. Deionized water was used to make all aqueous solutions. A typical run for preparing BFO powders is as follows: The 20 mL each of $Bi(NO_3)_3 \cdot 5H_2O$, $Fe(NO_3)_3 \cdot 9H_2O$, and $Al(NO_3)_3 \cdot 6H_2O$ were put into an 80-mL stainless steel autoclave and mixed well. After then, an appropriate amount of KOH solution was slowly dripped to the previous mixture solution until 65–80% of its volume was filled, which was next transferred into the strong magnetic stirring apparatus to stir for 2~3 h at 80 °C to get a clear solution. According to the method procedure, the obtained dark brown solution was transferred into Teflon-lined stainless steel autoclave. The hydrothermal treatment was carried out at a temperature of 200 °C for 10 h under autogenous pressure. The heating rate was 2 °C/min. After the hydrothermal reaction was complete, the resultant products were cooled down to RT naturally. Subsequently, the resultant powders were collected and washed several times with acetone, deionized water, and ethanol until the pH value of the solutions reached 7. Finally, the BFA_xO powders were placed in a thermostat drying oven for 6 h at 70 °C, and then dried for further characterization. We have prepared four sets of samples of BFA_xO by varying the concentration of $Al(NO_3)_3 \cdot 6H_2O$ from 0–0.1 M.

The crystal structure of BFA_xO samples was determined by X-ray diffraction (XRD, Mac Science M18XHF22-SRA). Raman spectroscopy (Renishaw InVia Reflex) with radiation from an Ar+ laser was employed to determine the structural properties of the powders at

RT. XAFS data were collected in the transmission mode at various concentrations at the beamline 1W2B of the Beijing Synchrotron Radiation Facility (BSRF), China. Fe K-edge spectrum with an energy resolution of $\Delta E/E$:2 × 10^{-4} and Bi L_3-edge spectrum with an energy resolution of $\Delta E/E$:1 × 10^{-4} were measured for the BFA$_x$O samples at RT. In order to obtain best XAFS data, BFA$_x$O powders were ground in an agate mortar, then mixed with BN and finally pressed into pellets. The background correction, normalization, and pre-edge and post-edge region of the absorption spectrum were fitted by ATHENA, a software for XAFS data processing, within the IFEFFIT program [33]. The E_o value was determined by the maximum in the first derivative in the edge region. We extracted the $\chi(k)$ profile in the k space of 0–12 Å^{-1}. The $k^3 \times \chi(k)$ profile was Fourier transformed to the R space of 0–8 Å, by using the Hanning window function. The Fe$_2$O$_3$ and Bi$_2$O$_3$ were measured as the reference compounds. The optical properties of the powders were evaluated using ultraviolet-visible spectrophotometer (UV-Vis, UV 3900H). In this work, the investigation is limited to the low doping concentration of $0 \leq x \leq 0.1$.

Results and Discussion

The XRD patterns of the undoped BFO ($x = 0$) and BFA$_x$O powders, which scanned from 2θ value of 15–60°, are shown in Fig. 1. The full spectra of XRD patterns in Fig. 1a indicate that all samples can be identified as the standard diffraction data of the corresponding rhombohedral distorted perovskite structure (JCPDS Card File No. 20-0169, space group: $R3c$). It can also be seen that all samples exhibit neat diffraction patterns with a small amount of secondary phases. Traces of a secondary phase can be seen at 27.6° and 32.8° (marked "*" for Bi$_2$Fe$_4$O$_9$ and "#"for Bi$_{25}$FeO$_{40}$) for $x = 0.5$ and $x = 0.1$ samples which may be resulting from the volatilization nature of Bi at the high sintering temperature [34]. This is often observed in the BFO powders synthesized by different routes [35–37]. Secondary phases are found to increase continuously at the high doping value. Therefore, B-site Al substitution for Fe cannot promote the pure phase of BFO; however, the electrical properties of samples would not be affected. From Fig. 1a, it can be seen that all diffraction peaks for the doped samples first shift to higher 2θ values with Al doping. For clarity, a part of XRD patterns in the 2θ region of 21 to 24° are amplified in Fig. 1b. From this enlarged view of the diffraction peaks, it can be observed that the (101) diffraction peak has an obvious shift toward high 2θ values with respect to undoped BFO, which confirms that Al is successfully doped into B-site of BFO. In analogy with undoped BFO, the (101) diffraction peak for the doped samples undergoes a shift in higher 2θ values first then small shift in lower 2θ values when $x = 0.1$ (surrounded by a dash line), as shown in
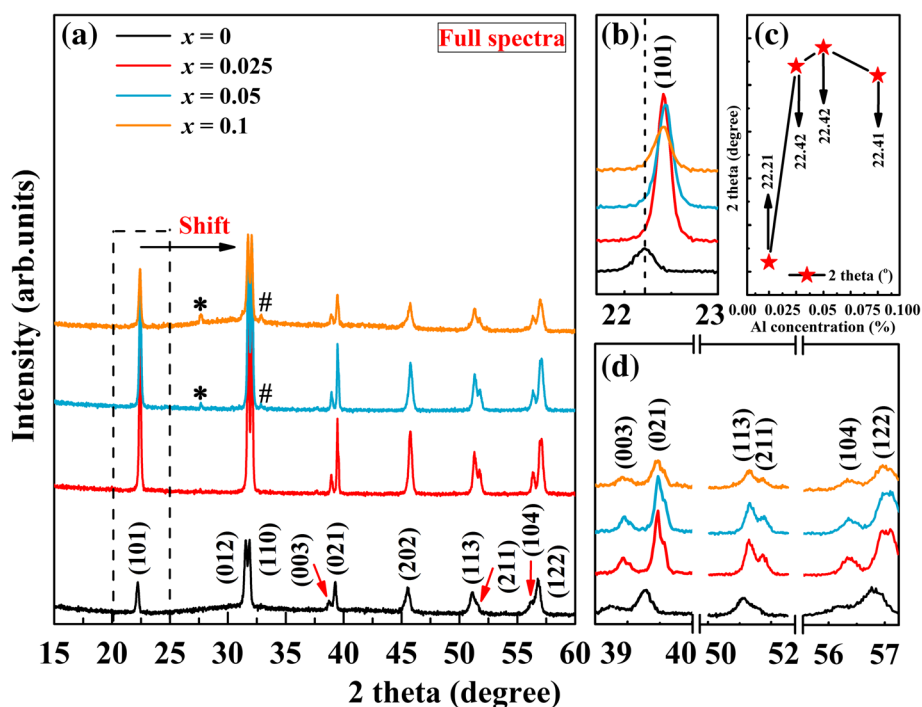

Fig. 1 a XRD patterns of BFA$_x$O ($0 \leq x \leq 0.1$). **b** Enlarged view of the XRD patterns in the range of 21–24°. **c** The (101) peak position as a function of Al concentration. **d** Magnified XRD patterns in the vicinity of 37–40°, 50–52°, and 55–57°

Fig. 1c. Magnified XRD patterns in the vicinities of 37–40°, 50–52°, and 55–57° are given in Fig. 1d. There are some twin peaks, viz., (003) and (021), (113) and (211), (104) and (122), in the XRD spectrum. With the increase of Al content, the intensity of these peaks first increases then decreases when x reaches 0.1. As we know, the intensity of the peaks is usually related to the crystallinity. The decrease of the diffraction peaks indicates that the crystallinity of BFA$_x$O decreases. Since Al^{3+} (0.51 Å) has a smaller ionic radius than Fe^{3+} (0.65 Å), it is easily incorporated into the BFO lattice when the doping amount is small, but excessive doping ion makes the BFO lattice unstable. The reduced crystallinity may be due to the fact that Al favors the creation of more nucleation sites which, in turn, inhibit the growth of crystal grains. Decreased crystallinity has also been found in other Al-doped BFO [28, 30]. On the other hand, this can occur if there is a creation of oxygen vacancies and transformation of some Fe^{3+} to Fe^{2+} due to the charge imbalance created in the system by Al^{3+} substitution. Similar phenomenon has been observed in Sr-doped BFO [38]. The shift in the diffraction peaks might be ascribed to the unit cell contraction, because of the small ionic radius of Al in comparison with Fe^{3+}. The results of XRD show that the trivalent Al^{3+} substitution in BFO does not lead to observable structural transformation.

The structure confirmed by XRD can also be characterized by the position and intensity of Raman active modes. Raman spectrum is sensitive to the atomic displacement and distribution. The Raman scattering spectra of the undoped BFO and BFA$_x$O powders are given in Fig. 2. On the basis of group theory, the 13 optical-phonon Raman active modes and 5 inactive modes (i.e., $5A_2$) of BFO are predicted for the rhombohedral distortion perovskites with space group *R3c* [39]. The theoretical analysis of the lattice vibrations in the perovskite *R3c* structure is as follows:

$$\Gamma_{R3c} = 4A_1\left(z, \ x^2, y^2, \ z^2\right) + 5A_2(-) \quad (1)$$
$$+ 9E\left(x, \ y, \ x^2 - y^2, \ xy, \ xz, \ y\right)$$

where A is longitudinal optical (LO) mode and E is the transverse optical mode (TO). In the full spectra shown in Fig. 2a, the number of clearly seen Raman active modes at RT is much less than predicted. In this work, we have observed six Raman active modes ($3A_1$(LO) + $3E$(TO)) for BFA$_x$O powders. This may be due to the accidental degeneracies between bands in the spectra and the inability to distinguish weak bands from background noise [40], or dielectric leakage in the sample. For the undoped BFO, the strong and wide peaks at 68.7 cm^{-1},
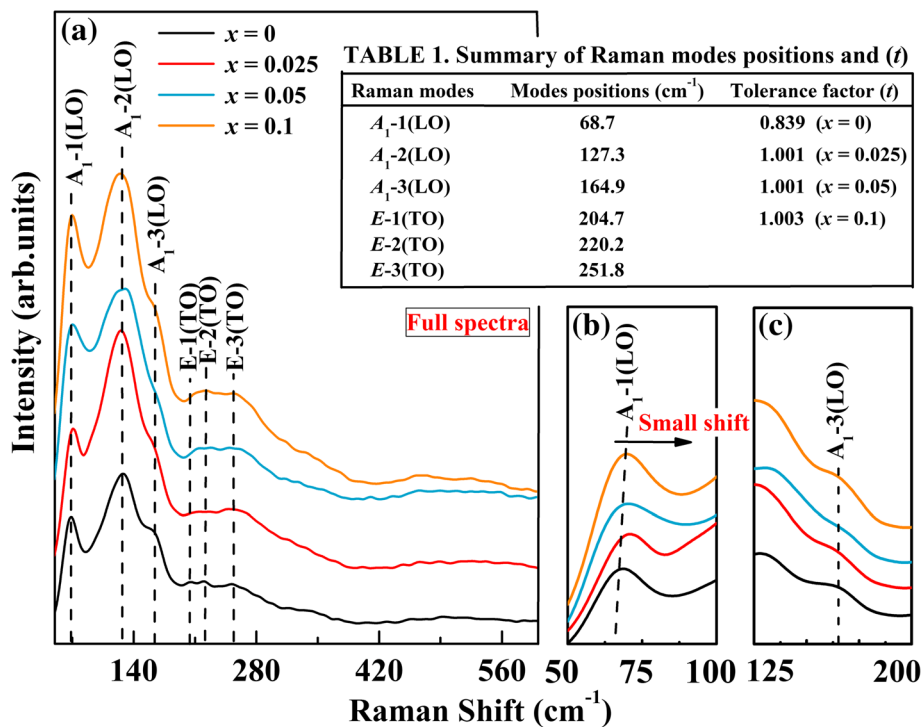

TABLE 1. Summary of Raman modes positions and (*t*)

Raman modes	Modes positions (cm^{-1})	Tolerance factor (*t*)
A_1-1(LO)	68.7	0.839 (*x* = 0)
A_1-2(LO)	127.3	1.001 (*x* = 0.025)
A_1-3(LO)	164.9	1.001 (*x* = 0.05)
E-1(TO)	204.7	1.003 (*x* = 0.1)
E-2(TO)	220.2	
E-3(TO)	251.8	

Fig. 2 a Raman spectrum of BFA$_x$O ($0 \leq x \leq 0.1$). **b** Enlarged Raman spectrum in the ranges of 50–100 cm^{-1} and **c** 125–200 cm^{-1}

127.3 cm^{-1}, and 164.9 cm^{-1} were assigned to A_1-1(LO), A_1-2(LO), and A_1-3(LO) modes, respectively. Peaks at 204.7 cm^{-1}, 220.2 cm^{-1}, and 251.8 cm^{-1} were assigned to E-1(TO), E-2(TO), and E-3(TO) modes, respectively (see Table 1 in Fig. 2). From the spectra, it can be clearly seen that these E(TO) modes are invisible. It is known that A_1-1(LO) modes are attributed to the Bi-O bonds, while the tilt A_1-3(LO) modes are viewed as the FeO$_6$ octahedron. E(TO) modes are assigned to the Fe-O vibration [41]. The Raman result confirms that the prepared undoped BFO belongs to the rhombohedral distorted perovskite structure with space group *R3c*. It is noted that all four samples show similar Raman pattern and vibration modes. This indicated the same rhombohedral *R3c* space group, but their intensities and frequencies were somewhat different. At the whole view of Raman pattern of BFA$_x$O samples, the peak position of the A_1-1(LO) modes is slightly shifted to a higher frequency and the peaks of A_1-3(LO) modes were broadened, indicating that the dopant Al is going to the B-site of BFO. The intensities of the E-1(TO), E-2(TO), and E-3(TO) modes are found to be slightly increased for the doped samples. For clarity, the A_1-1(LO) and A_1-3(LO) modes in the region of 50–100 cm^{-1} and 125–200 cm^{-1} are shown in Fig. 2b and c. From this enlarged spectrum, it is clear that A_1-1(LO) modes exhibit a small shift to higher frequencies with increasing Al content. Compared to those of the undoped BFO, the peaks for A_1-3(LO) modes were broadened for the doped samples. The small shift of the A_1-1(LO) modes, slight broadening of A_1-3(LO) modes, and change of the intensities of some E(TO) modes may be related to the change of the Bi-O and Fe-O covalent bonds and a compressive stress in the Al-doped sample [42, 36]. On the other hand, it is possible that all the above changes could be due to the fact that the B-site Fe^{3+} ions have been partially substituted by Al^{3+} ions. Apparently, these Raman results are consistent with the XRD observations. The Goldschmidt tolerance factor (t) is widely used to assess the geometric stability and distortion of crystal structures [43], where t is defined by the ratio of three kinds of ionic radii, as follows:

$$t = \frac{(r_A + r_O)}{\sqrt{2}\,(r_B + r_O)} \tag{2}$$

where r_A is the radius of Bi^{3+}, r_B is the average radii of Fe^{3+} and Al, and r_O is the radius of O^{2-}. However, the radii of Al and Fe^{3+} are 0.51 Å and 0.65 Å, while the Bi^{3+} and O^{2-} have the radii of 1.03 Å (according to Ref. [44]) and 1.38 Å, respectively. The t values for our studied perovskite composites BFA$_x$O are found to be 0.839, 1.001, 1.001, and 1.003 for x = 0, 0.025, 0.05, and 0.1, respectively (see Table 1 in Fig. 2). The ideal ABO$_3$

compounds adopt a cubic close-packed structure when the value of t is 1, while when $t < 1$ or > 1, a geometric strain arises [45, 46]. As the Al concentration increases, the average B-site ionic radius decreases, which leads to a further increase in the t value from 0.839 to 1.003. This may be due to the small change in a low symmetric state of BFO. It is well known that the B-site cation in perovskite is surrounded by six oxygen anions, and when replaced by smaller ions, the coordination distance will decrease. Hence, to clearly analyze the effects of the Al substitution, it is necessary to study the local electronic structure of the BFA$_x$O samples.
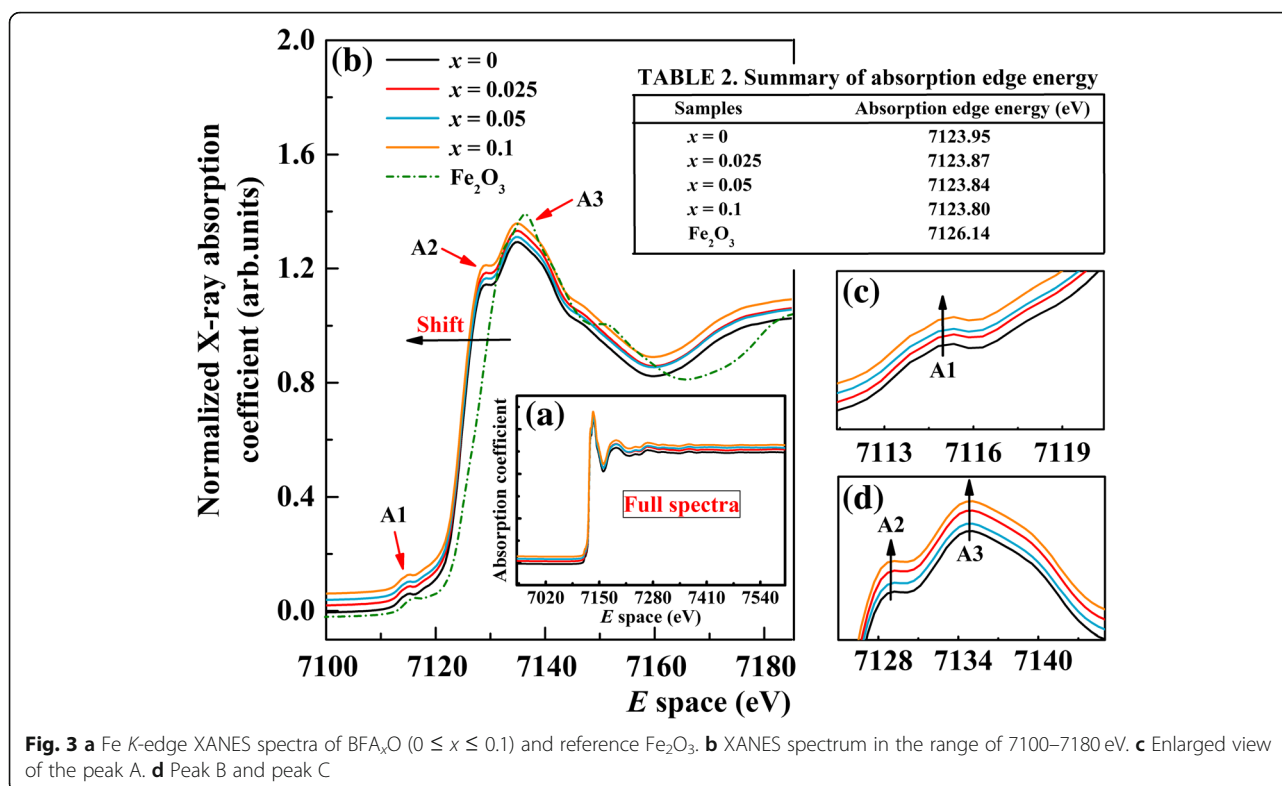
XAFS is divided into two types, i.e., X-ray absorption near edge structure (XANES) and extended X-ray absorption fine structure (EXAFS). In this measurement, when the X-ray penetrates through the slab with distance x, the intensity of the X-ray beam will be reduced to $I = I_o e^{-\mu x}$. XAFS measures the absorption of X-rays as a function of X-ray energy E, that is, the X-ray absorption coefficient $\mu(E) = -d \ln I/dx$ is determined from the decay in the X-ray beam intensity I with distance x [47]. The ratio of I/I_o is plotted as a function of E above the thresholds Fe K-edge (7112 eV) and Bi L_3 (13,419 eV), which can provide important information about the shape of the $\mu(E)$. The electronic transitions shall be following the dipole selection rule. An X-ray absorbance $\mu(\omega)$ can be obtained by Fermi's golden rule, as follows:

$$\mu(\omega) \propto \sum_f |\langle f|D|i\rangle|^2\, \delta\langle E_i - E_f + \omega\rangle \tag{3}$$

where $|i\rangle$ is the initial state, $|f\rangle$ is the final state, D is the dipole operator, E_i is the energy of $|i\rangle$, E_f is the energy of $|f\rangle$, and ω is the photon frequency. The XANES features contain useful information that are associated with the electronic structure of the absorber and local environment of an atomic structure. XANES function $\chi(E)$ is defined as follows:

$$\chi(E) = \left[\frac{\mu(E) - \mu_o(E)}{\Delta\mu_o}\right] \tag{4}$$

where $\mu_o(E)$ is the smooth atomic-like background and $\Delta\mu_o$ is a normalization factor that arises from the net increase in the total atomic background absorption edge. The standard Eq. (4) was used for the background subtraction and removal during the processing of XANES data. Firstly, a smooth pre-edge function is subtracted to remove the background from the instruments. Secondly, $\mu(E)$ is normalized and then a smooth post-edge background function is subtracted from the $\mu(E)$ to obtain the $\mu_o(E)$. Figure 3a shows the full spectra of the Fe K-edge XANES of an undoped BFO and BFA$_x$O powders along with the reference compound Fe$_2$O$_3$ investigated

Fig. 3 a Fe *K*-edge XANES spectra of BFA$_x$O (0 ≤ *x* ≤ 0.1) and reference Fe$_2$O$_3$. **b** XANES spectrum in the range of 7100–7180 eV. **c** Enlarged view of the peak A. **d** Peak B and peak C

in this work, while Fig. 3b reports the XANES spectrum in the energy range of 7100–7180 eV. From Fig. 3b, it can be seen that the shape of all spectra and peak positions is similar to each other. The absorption edges slightly shift toward lower energies with increasing Al concentration, which can be attributed to the chemical shift effect. The absorption edge energy shifts to lower energy with decreasing charge state, suggesting a complex bond configuration at the B-site. It is well known that edge shift could be used to obtain a mean oxidation state. The absorption edge energies for our studied samples BFA$_x$O are found to be 7124.95 eV, 7123.87 eV, 7123.84 eV, and 7123.80 eV for *x* = 0, 0.025, 0.05, and 0.1, respectively. For the reference compound Fe$_2$O$_3$, the absorption edge energy is 7126.14 eV (see Table 2 in Fig. 3). The absorption edge of doped samples is lower than that of the Fe$_2$O$_3$ (Fe^{3+}) reference compound. Increasing *x* values leads to the gradual shift of the absorption edge toward that of FeO (Fe^{2+}) [48]. From this, we can note that BFA$_x$O is a mixed-valent (Fe^{3+}/Fe^{2+}) system. In another aspect, three major features, pre-edge peak A1 and post-edge peaks A2 and A3, are observed in all four samples. The pre-edge peak A1, typical for BFO, corresponds to the electric quadrupole-forbidden transition from the O 1*s* level to Fe 3*d* ones, with a small admixture of Al 3*d* states. As the Al concentration increases,

the intensity of the pre-edge peak A1 exhibits a small increase for the doped samples (see Fig. 3c). The post-edge peak A2 is attributed to the O 2*p* band transfer to the Fe 3*d* orbit, the so-called ligand-to-metal charge transfer process [49], whereas peak A3 is caused by the 1*s* to 4*p* dipole-allowed transition [50]. With increasing Al concentration, the intensity of these two post-edge peaks can be clearly seen to increase for the doped samples (see Fig. 3d). All the above changes in pre-edge and post-edge peak intensity can be understood in terms of competition between hybridization of Fe 3*d* and Al 3*d* with O 2*p* orbitals. Besides, after Al ion doping, there are more unoccupied 4*p* orbitals occurring in BFA$_x$O. Except these, the whole spectra do not show significant changes and these results prove that Al ions are partially doped into B-site of BFA$_x$O.

The Fe-O, Fe-Fe/Al (i.e., Fe-O-Fe/Al), and Bi-O bond distributions are obtained by fitting the k^3-weighted ($k^3 \times \chi(k)$) raw data, as follows:

$$k = \sqrt{\frac{2m(E-E_o)}{\hbar}} \tag{5}$$

where E_o is the absorption edge energy and $\hbar$ is the Planck constant. Further fitting (some approximations

and oscillations) is made using the standard EXAFS equation, as follows:

$$\chi(k) = \sum_R S_o^2 N_R \frac{|f(k)|}{kR^2} \sin(2kR + 2\delta_c + \phi) e^{\frac{-2R}{\lambda(k)}} e^{-2\sigma^2 k^2}$$

(6)

where S_o^2 ($0 < S_o^2 < 1$) is the reduction factor, N_R is the number of backscattering atoms at distance R, $f(k)$ is the backscattering amplitude, δ_c is the phase shift from central, ϕ is the backscattering atoms, λ is the core-hole lifetime, σ^2 is the Debye-Waller factor from multiple distances, and k is the photoelectron mean free path. The EXAFS region is typically referred to the energy range of 20–30 eV above the edge jump, which is sensitive to short-range order types, bond distances, and coordination numbers in materials. Although, Eq. (6) could give some information about the EXAFS approximations and oscillations, it is not a particularly convenient form for visualizing the information content of an EXAFS spectrum. Therefore, Fourier transformation can be used to decompose a k space signal into its different constituent frequencies [32]. Fourier transformation is a complex function of interatomic distance R, the amplitude of which is represented by the real function of $\chi(R)$. In this function, the position of peaks is related to bond distances and neighboring ions. Equation (6) can be transformed from k space to R space by Fourier transform, as follows:

$$\chi(R) = \frac{1}{\sqrt{2\pi}} \int_{k_{\min}}^{k_{\max}} \omega(k) k^n \chi e^{-2ikR} dk$$

(7)

$$\begin{cases} 0 & k < k_{\min} \\ \sin^2\left[\frac{\pi(k-k_{\min})}{2(k_2-k_{\min})}\right] & k_{\min} < k < k_2 \\ 1 & k_2 < k < k_3 \\ \cos^2\left[\frac{\pi(k-k_3)}{2(k_{\max}-k_3)}\right] & k_3 < k < k_{\max} \\ 0 & k > k_{\max} \end{cases}$$

(8)

where $k_{\max}$ and $k_{\min}$ are the maximum and minimum values of transformed k space, respectively, $\chi(R)$ is the Hanning window function, $\omega(k)$ is the Gaussian window function, and k^n is the weight factor ($n = 0, 1, 2, 3$). The k_2 and k_3 values for the BFA$_x$O are 2 and 10, respectively, and the value of n is 2. Fourier transform of Fe K-edge EXAFS of the BFA$_x$O samples is performed, as shown in Fig. 4a. The asymmetric peak (surrounded by the first dash line) centered at ~ 1.503 Å is identified as a Fe-O bond, owing to scattering from the oxygen anions. The second strong peak (surrounded by the second dash line) around ~ 3.527 Å is corresponding to the Fe-Fe/Al bonds, which can be explained by the scattering of oxygen anions from the next-to-nearest-neighboring Fe/Al atomic shells. The distance for the first and second coordination shells has been summarized in Table 3 in Fig. 4. From the peak position, compared with undoped
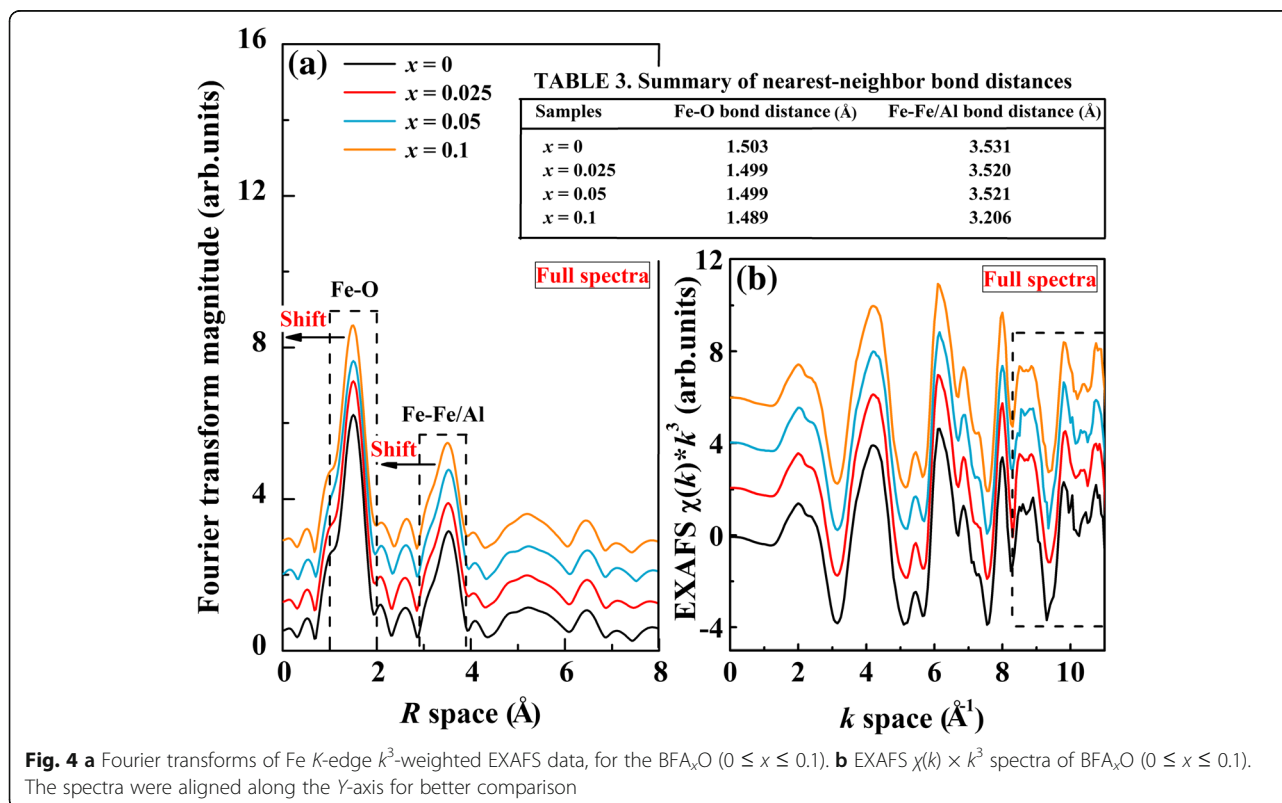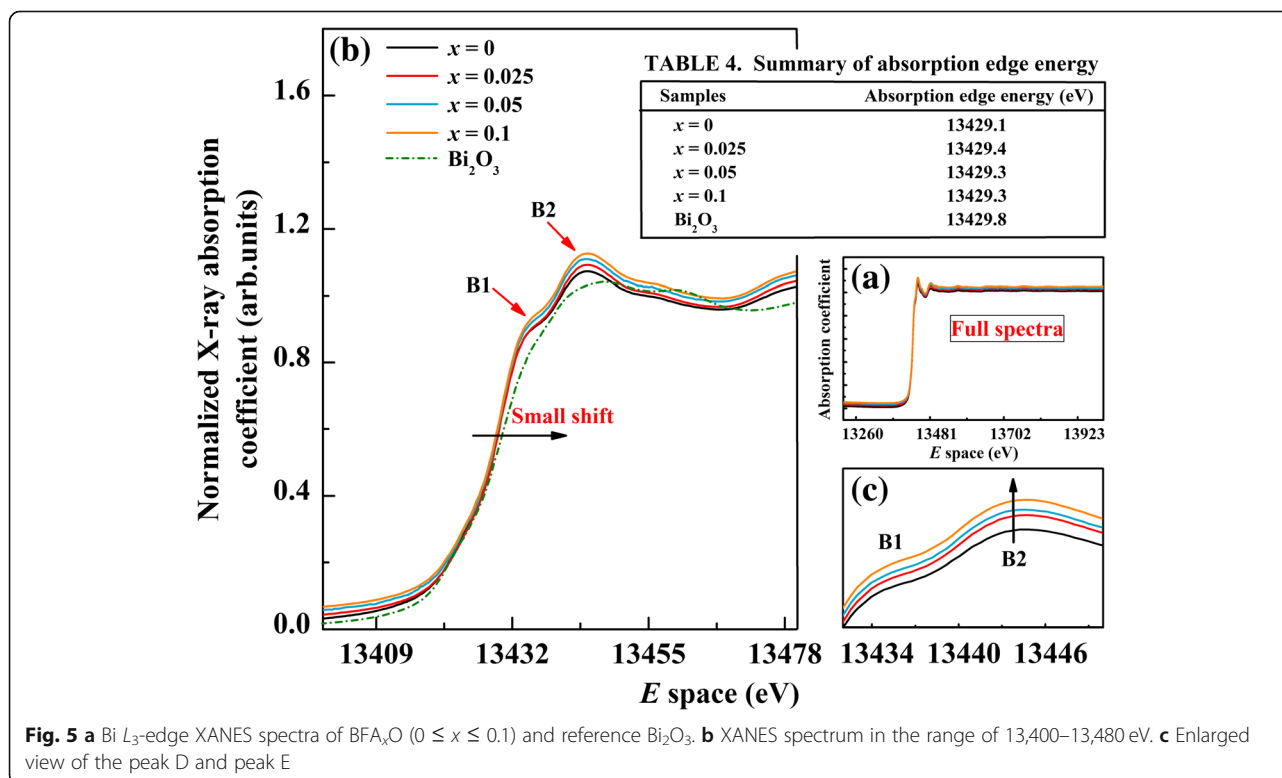

Fig. 4 a Fourier transforms of Fe *K*-edge k^3-weighted EXAFS data, for the BFA$_x$O ($0 \leq x \leq 0.1$). **b** EXAFS $\chi(k) \times k^3$ spectra of BFA$_x$O ($0 \leq x \leq 0.1$). The spectra were aligned along the *Y*-axis for better comparison

TABLE 3. Summary of nearest-neighbor bond distances

Samples	Fe-O bond distance (Å)	Fe-Fe/Al bond distance (Å)
$x = 0$	1.503	3.531
$x = 0.025$	1.499	3.520
$x = 0.05$	1.499	3.521
$x = 0.1$	1.489	3.206

Gholam *et al. Nanoscale Research Letters* (2019) 14:137

Page 8 of 12

BFO sample, Fe-O and Fe-Fe/Al bond tends to slightly shift toward smaller R values with increasing x. This indicates that doping by Al ions not only affects the nearest-neighbor local structure of central Fe atom but also affects the next-nearest coordination shells of the Fe atom. On the other hand, the shift of the Fe-O bond to smaller R values may result from that the radius of Al ions is smaller than that of Fe ions. This is consistent with the XRD data. The shift of Fe-Fe/Al to smaller R values also indicates that the average Fe-Fe/Al bond length (where the two Fe^{3+} ions are in the centers of neighboring oxygen octahedral) gradually becomes shorter and the bond angle is modified in the Al-doped samples. However, there is a small increase of peak intensity of the Fe-O distribution for the doped samples while the peak intensity of the Fe-Fe/Al distribution is almost not changed. This reveals that the iron-neighboring structure of Fe-O has been modified by Al doping. The shorter Fe-Fe/Al bonds in Al-doped samples can explain why the major peaks (101) in XRD shift to higher 2θ angles (see Fig. 1b). This indicates that the substitution of Al for Fe could affect oxygen octahedral, which further reduces the coordination distance between the two neighboring Fe atoms. Figure 4b shows the Fe K-edge EXAFS of the BFA$_x$O samples processed on $k^3 \times \chi(k)$ oscillation with a k space of 0–10 Å^{-1}. As can be seen, all the $k^3 \times \chi(k)$ spectra show similar patterns at the smaller k values but different at larger k values with some various noise (surrounded by the dash line).

Al-doped samples show a broader $k^2 \times \chi(k)$ spectrum than those of undoped BFO in the k space of 8.2–9.3 Å^{-1}, implying an enhanced short-range structural disorder in BFA$_x$O samples. The noises are observed in a k space of 10–10.4 Å^{-1}. These changes indicated that the local structure of center atoms has changed due to B-site Al doping, similar to what was reported by Li et al. [51].

The peak positions, intensities, and shapes of the line in the Bi L_3-edge XANES spectrum are well known to depend on the local electronic structure of the Bi atoms, which could provide information on the Bi valence. The full spectra of Bi L_3-edge XANES of undoped BFO and BFA$_x$O samples are also shown in Fig. 5a, while Fig. 5b shows the Bi L_3-edge XANES spectrum in the energy region of 13,400–13,480 eV. The analysis of these spectra helps to investigate the local electronic structure of Bi ions in the doped system. From Fig. 5b, it can be seen that the shape of all spectra are the same to each other and there is almost no change of absorption edge in the whole series. The absorption edge energies for our study are found to be 13,429.1 eV, 13,429.4 eV, 13,429.3 eV, 13,429.3 eV, and 13,429.8 eV for x = 0, 0.025, 0.05, and 0.1 and the reference compound Bi_2O_3, respectively (see Table 4 in Fig. 5). The absorption edges slightly shift toward higher energies with increasing Al concentration. The absorption edge in the Bi L_3-edge of the BFA$_x$O samples matches well with that of the reference compound Bi_2O_3, which indicates that the valence state of Bi

Fig. 5 a Bi L_3-edge XANES spectra of BFA$_x$O ($0 \le x \le 0.1$) and reference Bi_2O_3. b XANES spectrum in the range of 13,400–13,480 eV. c Enlarged view of the peak D and peak E

ions in all the samples is in + 3 valence state. However, there are two post-edge peaks found in all samples and marked as B1 and B2, respectively. These two post-edge peaks are caused by the electric-forbidden transition from $2p_{3/2}$ level to the $6d$ ones. Compared with undoped BFO, the intensity of peak B2 can be clearly seen to increase for the doped samples (see Fig. 5c), which means the transition from $2p_{3/2}$ to $6d$ state increases, so does the energy of $6d$ state. Except these, there is no other significant change in the whole spectrum.

Fourier transform of Bi L_3-edge EXAFS radial distribution functions is performed, as shown in Fig. 6a. A high-intensity peak located at around 1.618 Å corresponds to the nearest Bi-O coordination shell (surrounded by the dash line), which is a result from scattering from the nearest-neighbor atomic shell of Bi, i.e., oxygen anions. However, the position of Bi-O bond shifts toward larger R values for the doped samples (see Table 5 in Fig. 6). This indicates that the substitution of Al for Fe could affect the nearest-neighbor local structure of the central Bi atom. It also indicates the extension of Bi-O bond length. The peak intensity of the Bi-O distribution exhibited a small increase with increasing Al content, which suggests that the iron-neighboring structure of Bi-O has changed. Figure 6b shows the Bi L_3-edge $k^3 \times \chi(k)$ EXAFS spectra with a k space of 0–14 Å^{-1}. From Fig. 6b, it can be seen that all the spectra shape shows similar patterns except some error noises. The error noises are observed in the k space of 12–14

Å^{-1} (surrounded by the dash line). This result may imply that the $k^3 \times \chi(k)$ EXAFS function of the center Bi atoms has changed with Al doping. This also suggests that the B-site Al substitution influences short-range structural disordering.

The optical properties of the samples are studied by using RT UV-Vis, which is used to characterize the optical properties of the materials. The UV-Vis absorption spectra of undoped BFO and BFA$_x$O samples in the wavelength of 300–800 nm are shown in Fig. 7a. As a result, the UV-Vis spectra of the undoped BFO and BFA$_x$O samples show two absorption edges (marked by dashed arrows). One is a band around 650 nm, which is due to the metal-to-metal transition. The other is a band around 760 nm, which is caused by crystal field transition [52]. In addition, the strong absorption band is observed at about 490 nm (marked by dashed arrow), which is attributed to the electronic transition from O $2p$ to Fe $3d$ state in the BFO. These strong bands indicate that the BFO prepared by hydrothermal method could be a promising visible-light photocatalytic material. BFO is of direct transition with a value of n as 2. The absorption edge of the doped samples shifted from 659 to 619 nm, suggesting that the BFA$_x$O powders absorb visible light in the wavelength range of 600–659 nm (see Fig. 7a). A similar blue-shift phenomenon was observed earlier in other element-doped BFO [53–55]. This blue shift in the absorption spectra of Al-doped samples in comparison with the undoped BFO shows that doping
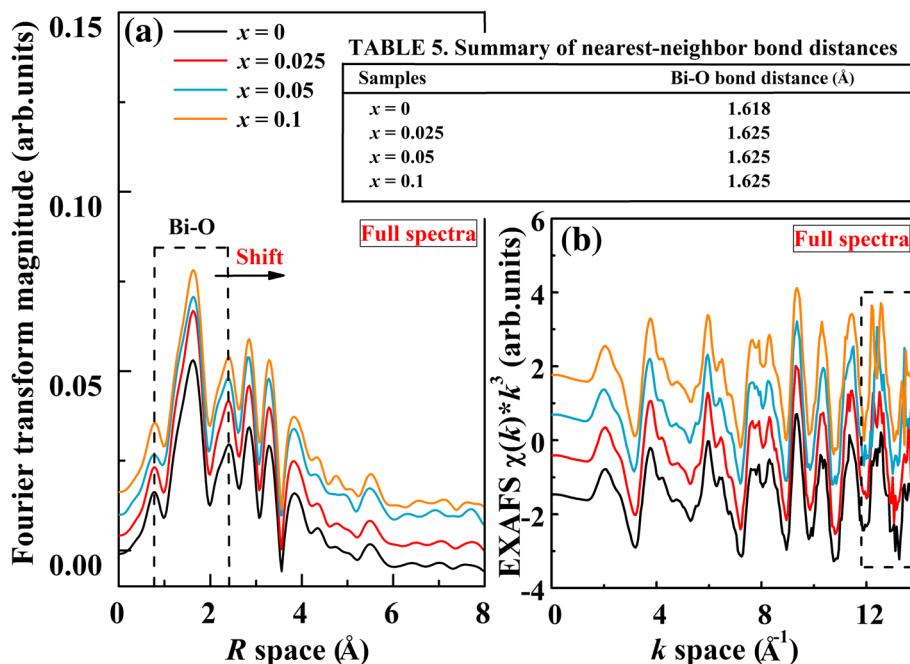

Fig. 6 a Fourier transforms of Bi L_3-edge k^3-weighted EXAFS data, for the BFA$_x$O (0 ≤ x ≤ 0.1). **b** EXAFS $\chi(k) \times k^3$ spectra of BFA$_x$O (0 ≤ x ≤ 0.1). The spectra were aligned along the Y-axis
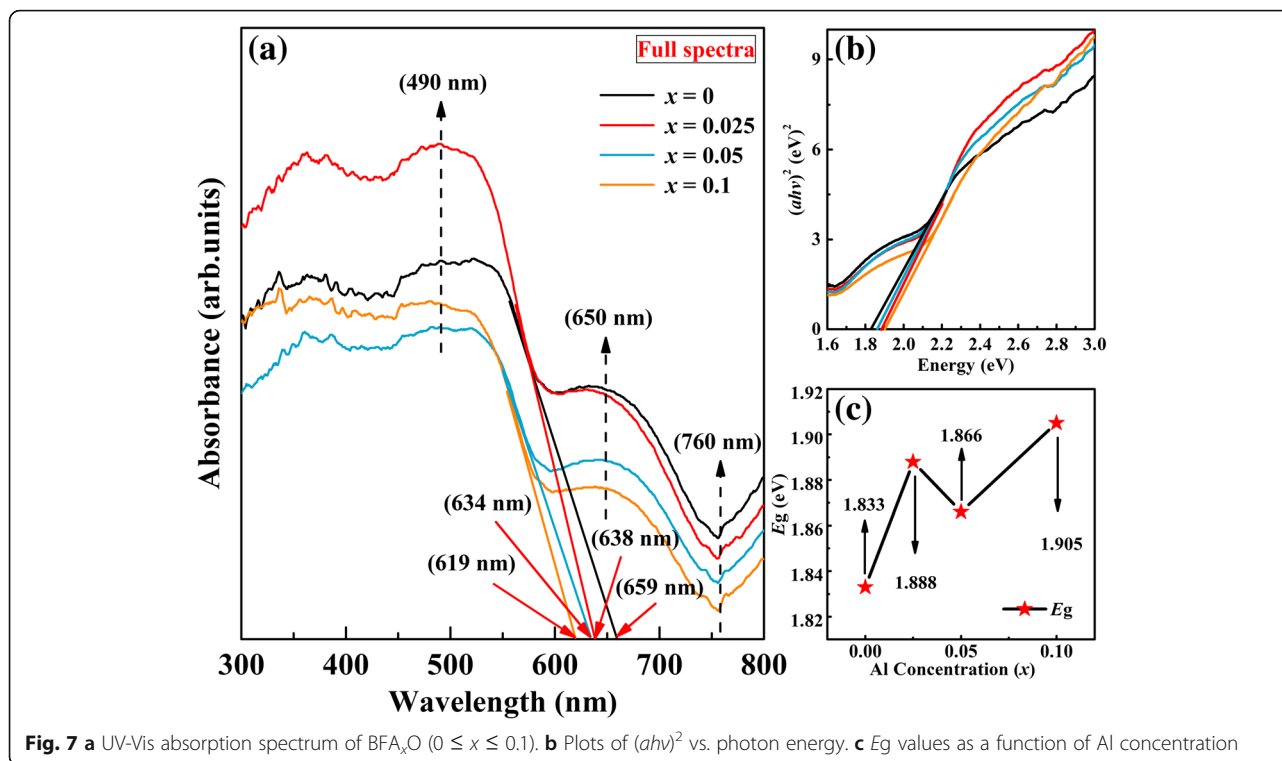
TABLE 5. Summary of nearest-neighbor bond distances

Samples	Bi-O bond distance (Å)
x = 0	1.618
x = 0.025	1.625
x = 0.05	1.625
x = 0.1	1.625

Gholam *et al. Nanoscale Research Letters* (2019) 14:137

Page 10 of 12

Fig. 7 a UV-Vis absorption spectrum of BFA$_x$O (0 ≤ x ≤ 0.1). **b** Plots of $(ahv)^2$ vs. photon energy. **c** Eg values as a function of Al concentration

Al causes a change in the local structure for BFO. From Fig. 7a, one can see that the absorption spectra of the Al-doped samples exhibit a sharp increase around 490 nm and it suggests that all samples can absorb remarkable amounts of visible light. For the sample with x = 0.025, the absorption spectrum shows a sudden increase. It means that it has a wider absorption range than the other samples in this range of visible light. The optical band gap of the samples has been calculated by Tauc's formula, as follows:

$$ahm = A(hm - Eg)^n \tag{9}$$

where a is the absorption coefficient, A is the parameter, h is the Planck's constant, m is the frequency of the incident photon, Eg is the optical band gap, and n (for direct n = 2, for indirect n = 0.5) is a constant associated with different types of electronic transitions, as shown in Fig. 7b. The calculated Eg values are found to be 1.833 eV, 1.888 eV, 1.866 eV, and 1.905 eV for x = 0, x = 0.025, x = 0.05, and x = 0.1 samples, respectively. It is easy to see that the band gap increases with the substitution ratio, as shown in Fig. 7c. The increase in the band gap is attributed to the doping effect. The Eg value for the undoped BFO is about 1.833 eV, which is lower than the previous reports [56, 57].

Conclusion

In summary, the BFA$_x$O (x = 0, 0.025, 0.05, and 0.1) multiferroic powder samples were successfully synthesized via hydrothermal route. Effects of Al substitution on the structural, electrical, and optical properties of the samples were studied. The structural study reveals that Al-doped BiFeO$_3$ shows the existence of secondary phases and lattice contraction due to lower ionic radii of Al doped into B-site, which still retains its rhombohedral $R3c$ perovskite structure. Raman scattering measurement infers six Raman active phonon modes, which further confirms the result of XRD. XAFS studies on the Fe K-edge and B L_3-edge of the BFA$_x$O samples and of the reference compounds Fe$_2$O$_3$ and Bi$_2$O$_3$ were performed, and the obtained results were compared in order to determine the valance states of Fe and Bi ions in the system. The Fe K-edge XAFS results revealed that BFA$_x$O is a mixed-valent (Fe^{3+}/Fe^{2+}) system. The results of Fe K-edge XAFS also illustrate a competition between the Fe 3d and Al 3d orbitals on hybridization with the O 2p and occurrence of the more 4p orbitals with Al doping. Besides, Al ion doping affects both the nearest-neighbor and next-nearest coordination shells of the Fe atom. The B L_3-edge XAFS results indicate that valence states of Bi ions in all the samples are in + 3 and the transition from 2$p_{3/2}$ to 6d state and the energy of 6d state increases. Substitution Al for Fe could affect the nearest-neighbor local structure of central Bi atom. The BFA$_x$O prepared by hydrothermal method could be an appropriate visible-light photocatalytic material due to a strong absorption band in the visible region.

Abbreviations
AFM: Antiferromagnetic; BFA$_x$O: BiFe$_{1-x}$Al$_x$O$_3$; BFO: BiFeO$_3$; EXAFS: X-ray absorption fine structure; FE: Ferroelectric; FM: Ferromagnetic; RT: Room temperature; UV-Vis: Ultraviolet-visible; XAFS: X-ray absorption fine structure; XANES: X-ray absorption near edge structure; XRD: X-ray diffraction

Availability of Data and Materials
The datasets are available from the authors on reasonable request.

Authors' Contributions
The work presented here was performed in collaboration of all the authors. TG carried out most of the measurement and analysis as well as writing the draft of the manuscript. LRZ, JOW, HJQ, and RW contributed to the synchrotron experiments. HQW provided the leading insights and revised the manuscript. All authors read and approved the final manuscript.

Competing Interests
The authors declare that they have no competing interest.

Publisher's Note
Springer Nature remains neutral with regard to jurisdictional claims in published maps and institutional affiliations.

Author details
[1]Key Laboratory of Semiconductors and Applications of Fujian Province, Collaborative Innovation Center for Optoelectronic Semiconductors and Efficient Devices, Department of Physics, Xiamen University, Xiamen 361005, People's Republic of China. [2]Beijing Synchrotron Radiation Facility, Institute of High Energy Physics, Chinese Academy of Sciences, Beijing 100049, People's Republic of China.

References
1. Wang J, Neaton JB, Zheng H, Nagarajan V, Ogale SB, Liu B, Viehland D, Vaithyanathan V, Schlom DG, Waghmare UV (2003) Epitaxial BiFeO$_3$ multiferroic thin film heterostructures. Cheminform 299:1719–1722
2. Spaldin NA, Fiebig M (2005) The renaissance of magnetoelectric multiferroics. Science 309:391–392
3. Zhang X, Sui Y, Wang X, Wang Y, Wang Z (2010) Effect of Eu substitution on the crystal structure and multiferroic properties of BiFeO$_3$. J Alloys Compd 507:157–161
4. Song SH, Zhu QS, Weng LQ, Mudinepalli VR (2015) A comparative study of dielectric, ferroelectric and magnetic properties of BiFeO$_3$ multiferroic ceramics synthesized by conventional and spark plasma sintering techniques. J Eur Ceram Soc 35:131–138
5. Miah MJ, Khan MNI, Hossain AKMA (2015) Synthesis and enhancement of multiferroic properties of (x)Ba$_{0.95}$Sr$_{0.05}$TiO$_3$-(1-x)BiFe$_{0.90}$Dy$_{0.10}$O$_3$ ceramics. J Magn Mater 397:39–50
6. Jia DC, Xu JH, Ke H, Wang W, Zhou Y (2009) Structure and multiferroic properties of BiFeO$_3$ powders. J Eur Ceram Soc 29:3099–3103
7. Yan F, Lai MO, Lu L, Zhu TJ (2010) Enhanced multiferroic properties and valence effect of Ru-doped BiFeO$_3$ thin films. J Phys Chem C 114:6994–6998
8. Yan F, Zhu TJ, Lai MO, Lu L (2010) Enhanced multiferroic properties and domain structure of La-doped BiFeO$_3$ thin films. Scripta Mater 63:780–783
9. Catalan G, Scott JF (2009) Physics and applications of bismuth ferrite. Adv Mater 21:2463–2485
10. Yan X, Tan G, Liu W, Ren H, Xia A (2015) Structural, electric and magnetic properties of Dy and Mn co-doped BiFeO$_3$ thin films. Ceram Int 41:3202–3207
11. Iorgu AI, Maxim F, Matei C, Ferreira LP, Ferreira P, Cruz MM, Berger D (2015) Fast synthesis of rare-earth (Pr^{3+}, Sm^{3+}, Eu^{3+} and Gd^{3+}) doped bismuth ferrite powders with enhanced magnetic properties. J Alloys Compd 629:62
12. Cotica LF, Estrada FR, Freitas VF, Dias GS (2012) Ferroic states in La doped BiFeO$_3$-PbTiO$_3$ multiferroic compounds. J Appl Phy 111:114105
13. Cen Z, Zhou C, Yang H, Zhou Q, Li W, Yuan C (2013) Structural, ferroelectric and piezoelectric properties of Mn-modified BiFeO$_3$-BaTiO$_3$ high-temperature ceramics. J Mater Sci-Mater El 24:3952–3957
14. Juan PC, Wang JL, Hsieh TY, Lin CL, Yang CM, Shye DC (2015) The physical and electrical characterizations of Cr-doped BiFeO$_3$ ferroelectric thin films for nonvolatile memory applications. Microelectron Eng 138:86–90
15. Reetu A, Agarwal S, Sanghi A (2011) Rietveld analysis, dielectric and magnetic properties of Sr and Ti codoped BiFeO$_3$ multiferroic. J Appl Phy 110:073909
16. Suresh P, Babu PD, Srinath S (2016) Role of (La, Gd) co-doping on the enhanced dielectric and magnetic properties of BiFeO$_3$ ceramics. Ceram Int 42:4176–4184
17. Rojas-George G, Concha-Balderrama A, Esparza-Ponce H, Silva J, Galindo JTE, Cruz MP, Gervacio JJ, Graeve OA, Herrera G, Fuentes L, Reyes-Rojas A (2016) Local polarization switching in Ba-Ni co-doped BiFeO$_3$ thin films with low rhombohedral-symmetry distortion. J Mater Sci 51:2283–2291
18. Mao WW, Wang XF, Chu L, Zhu YY, Wang Q, Zhang J, Yang JP, Li XA, Huang W (2016) Simultaneous enhancement of magnetic and ferroelectric properties in Dy and Cr co-doped BiFeO$_3$ nanoparticles. Phys Chem Chem Phys 18:6399–6405
19. Tang P, Kuang DH, Yang SH, Zhang YL (2016) The structural and magnetic properties of Bi$_{1-x}$Y$_x$Fe$_{1-y}$MnyO$_3$ particles synthesized via a sol-gel technique. Ferroelectrics 491:104–111
20. Sharma S, Shandilya M, Rai R (2015) Effect of Tb, Ti co-doping on the electrical and magnetic properties of (Bi, La)FeO$_3$ multiferroic ceramics. J Mater Sci-Mater El 26:9484–9494
21. Zhu Y, Quan C, Ma Y, Wang Q, Mao W, Wang X, Zhang J, Min Y, Yang J, Li Xa, Huang W (2017) Effect of Eu, Mn co-doping on structural, optical and magnetic properties of BiFeO$_3$ nanoparticles. Mat Sci Semicon Proc 57:178–184
22. Bernardo MS, Jardiel T, Peiteado M, Caballero AC (2016) Metastable nature of donor-doped BiFeO$_3$ obtained by mechanochemical synthesis. J Ceram Soc Jpn 124:92–97
23. Stojadinović B, Dohčević-Mitrović Z, Paunović N, Ilić N, Tasić N, Petronijević I, Popović D, Stojanović B (2016) Comparative study of structural and electrical properties of Pr and Ce doped BiFeO$_3$ ceramics synthesized by auto-combustion method. J Alloys Comp 657:866–872
24. Ramesh R, Al E et al (2003) Epitaxial BiFeO$_3$ multiferroic thin film heterostructures. Sci 299:1719–1722
25. Zhang N, Wei Q, Qin L, Chen D, Chen Z, Niu F, Wang J, Huang Y (2017) Crystal structure, magnetic and optical properties of Mn-doped BiFeO$_3$ by hydrothermal synthesis. J Nanosci Nanotechno 17:544–549
26. Zhang H, Kajiyoshi K (2010) Hydrothermal synthesis and size-dependent properties of multiferroic bismuth ferrite crystallites. J Am Ceram Soc 93:3842–3849
27. Yoshimura M, Byrappa K (2008) Hydrothermal processing of materials: past, present and future. J Mater Sci 43:2085–2103
28. Azam A, Jawad A, Ahmed AS, Chaman M, Naqvi A (2011) Compounds, structural, optical and transport properties of Al^{3+} doped BiFeO$_3$ nanopowder synthesized by solution combustion method. J Alloys Comp 509:2909–2913
29. Chennabasappa M, Bellakki M, Manivannan V (2010) Synthesis and characterization of doped BiFeO$_3$ materials for photocatalytic applications. J Mater Eng 17:131–139
30. Jawad A, Ahmed AS, Ashraf SSZ, Chaman M, Azam A (2012) Exploring the dielectric behaviour of nano-structured Al^{3+} doped BiFeO$_3$ ceramics synthesized by auto ignition process. J Alloys Comp 530:63–70
31. Wang YG, Yang LL, Wang YJ, Wang XF (2012) Hollow crystals of BiFeO$_3$ prepared via a Al^{3+}-assisted hydrothermal method. Appl Mechan Mater 174(177):516–519
32. Sayers DE, Stern EA, Lytle FW (1971) New technique for investigating noncrystalline structures: fourier analysis of the extended x-ray-absorption fine structure. Phys Rev Lett 27:1204–1207
33. Ravel B, Newville M (2005) ATHENA, ARTEMIS, HEPHAESTUS: data analysis for X-ray absorption spectroscopy using IFEFFIT. J synchrotron radiat 12:537–541
34. Eerenstein W, Mathur ND, Scott JF (2006) Multiferroic and magnetoelectric materials. Nature 442:759–765
35. Maître A, François M, Gachon JC (2004) Experimental study of the Bi$_2$O$_3$-Fe$_2$O$_3$ pseudo-binary system. J Phase Equilib Diff 25:59–67
36. Zheng XH, Ma ZH, Chen PJ, Tang DP, Ma N (2012) Decomposition behavior and dielectric properties of Ti-doped BiFeO$_3$ ceramics derived from molten salt method. J Mater Sci-Mater El 23:1533–1537

Gholam *et al. Nanoscale Research Letters*   (2019) 14:137

Page 12 of 12

37. Rao TD, Karthik T, Srinivas A, Asthana S (2012) Study of structural, magnetic and electrical properties on Ho-substituted BiFeO$_3$. Solid State Commun 152:2071–2077
38. Thakur S, Pandey OP, Singh KJCI (2014) Role of Sr^{2+} substitution on structural, thermal and conducting behavior of Bi$_{1-x}$Sr$_x$FeO$_3$ (0.40≤x≤0.55). Ceram Int 40:16371–16379
39. Singh MK, Jang HM, Ryu S, Jo MH (2006) Polarized raman scattering of multiferroic BiFeO$_3$ epitaxial films with rhombohedral R3c symmetry. Appl Phys Lett 88:042907
40. Matson DW, Sharma SK, Philpotts JA (1983) The structure of high-silica alkali-silicate glasses. A Raman spectroscopic investigation. J Non-Cryst Solids 58:323–352
41. Chang LY, Tu CS, Chen PY, Chen CS, Schmidt VH, Wei HH, Huang DJ, Chan TS (2015) Raman vibrations and photovoltaic conversion in rare earth doped (Bi$_{0.93}$RE$_{0.07}$)FeO$_3$ (RE=Dy, Gd, Eu, Sm) ceramics. Ceram Int 42:834–842
42. Singh MK, Ryu S, Jang HM (2005) Polarized raman scattering of multiferroic bifeo$_3$ thin films with pseudo-tetragonal symmetry. Phys Rev B 72:2101
43. Goldschmidt VM (1926) Die Gesetze der Krystallochemie. Naturwissenschaften 14:477–485
44. Liu W, Tan G, Xue X, Dong G, Ren H, Xia A (2014) Phase transition and enhanced multiferroic properties of (Sm, Mn and Cr) co-doped BiFeO$_3$ thin films. Ceram Int 40:12179–12185
45. Triana CA, Corredor LT, Téllez DAL, Roa-Rojas J (2011) High temperature-induced phase transitions in Sr$_2$GdRuO$_6$ complex perovskite. Mater Res Bull 46:2478–2483
46. Sato T, Takagi S, Deledda S, Hauback BC, Orimo S (2016) Extending the applicability of the Goldschmidt tolerance factor to arbitrary ionic compounds. Sci Rep 6:23592
47. Rehr JJ, Albers RC (2000) Theoretical approaches to x-ray absorption fine structure. Rev Mod Phys 72:621–654
48. Saxena P, Dar MA, Sharma P, Kumar A, Varshney D (2016) Structural, dielectric and ferroelectric properties of La and Ni codoped BiFeO$_3$. J Appl Phys 1728:020307
49. Lee D, Kim MG, Ryu S, Jang HM, Lee SG (2005) Epitaxially grown La-modified BiFeO$_3$ magnetoferroelectric thin films. Appl Phys Lett 86:222903
50. Westre TE, Kennepohl P, DeWitt JG, Hedman B, Hodgson KO, Solomon EI (1997) A multiplet analysis of Fe K-edge 1s→3d pre-edge features of iron complexes. J Am Chem Soc 119:6297–6314
51. Gong L, Zhou Z, Wang S, Wang B (2013) Preparation and characterization of BiFeO$_3$@Ce-doped TiO$_2$ core-shell structured nanocomposites. Mater Sci Semicon Proc 16:288–294
52. Xiao YG, Zhong WQ, Deng ZY, Yan FS, Jin L (2015) Investigation on structural and functional properties of Nd doped BiFeO$_3$ particles prepared by hydrothermal method. J Mater Sci-Mater El 26:1–7
53. Jian H, Guo R, Liang F, Wen D, Zheng F, Shen MJMRB (2013) Characterization and visible light photocatalytic mechanism of size-controlled BiFeO$_3$ nanoparticles. Mater Res Bull 48:3017–3024
54. Quan C, Ma Y, Han Y, Tang X, Lu M, Mao W, Jian Z, Yang J, Li XA, Wei A (2015) Effect of Nd substitution for Ca on crystal structure, optical and magnetic properties of multiferroic Bi$_{0.9}$Ca$_{0.1}$FeO$_3$. J Alloys Comp 635:272–277
55. Sharma S, Singh V, Kotnala RK, Dwivedi RKJJoMSMiE (2014) Comparative studies of pure BiFeO$_3$ prepared by sol-gel versus conventional solid-state-reaction method. J Mater Sci-Mater El 25:1915–1921
56. Fu C, Sun F, Hao J, Gao R, Cai W, Chen G, Deng X (2016) The growth, enhanced optical and magnetic response of BiFeO$_3$ nanorods synthesized by hydrothermal method. J Mater Sci-Mater El 27:8242–8246
57. Anshul A, Borkar H, Singh P, Pal P, Kushvaha SS, Kumar A (2014) Photoconductivity and photo-detection response of multiferroic bismuth iron oxide. Appl Phy Lett 104:132910